ELSEVIER

Precession electron diffraction: Observed and calculated intensities

P. Oleynikov*, S. Hovmöller, X.D. Zou

Structural Chemistry, Arrhenius Laboratory, Stockholm University, Svante Arrhenius v., 12 SE 106 91 Stockholm, Sweden

Abstract

Theory and algorithms have been developed for performing kinematical and dynamical two-beam and multibeam dynamical simulations of precession electron diffraction patterns. Intensities in experimental precession patterns have been quantified and are shown to be less dynamical.
© 2007 Elsevier B.V. All rights reserved.

Keywords: Precession electron diffraction; Electron crystallography; Multislice simulation

1. Introduction

Electron crystallography emerges as a new tool for accurate structure determination of very small crystals. In order to exploit the full potential of electron diffraction, the methods for data acquisition and processing have to be developed towards the high standards of X-ray crystallography. Spot diffraction patterns give complete separation of reflections and provide two- or three-dimensional data sets.

One main goal of electron crystallography is to determine atomic structures quantitatively. Electron diffraction as a method of structure analysis has its own special possibilities and advantages in comparison with X-ray diffraction. Simultaneously, X-ray powder diffraction has gained in popularity partly because of the big transformation of the method as a consequence of several important developments. This is often possible because of the power and availability of computers.

Vincent and Midgley at the University of Bristol developed the precession technique in 1994. It has recently become more available to the TEM users because of hardware implementations. Precession allows data acquisition of sufficient quality for structure determination. Dynamical interactions can be effectively reduced (see for example Refs. [1–3]) using the precession method, and the

intensity data can be treated at first steps within the kinematical approximation in order to get a structure model by direct methods for example. An analysis of Lorentz corrections in precession diffraction have been previously published by Gjonnes [4], and the role of dynamical diffraction effects in precession via a Blackman model with Bethe potential corrections has been given by Gjonnes et al. [5]. The use of multislice to simulate precession diffraction intensities, the various different Lorentz correction terms, the effects of breakdowns of the Blackman approximation, how the results depend upon the scattering angle and the differences between kinematical, two-beam and multislice results including *R*-factor analyses are discussed in the Ph.D. thesis of Own [6], see also Own et al. [7] and the references therein for further details. However, a deeper understanding of the theory is necessary.

2. Precession electron diffraction

In the condition with precessing electron beam, the incident beam, which can be parallel or convergent, is tilted away from the zone axis to some angle. This angle is called precession angle and is typically 1–3°. In case of 1° precession inclination, the reciprocal resolution of the outermost reciprocal points within the zero-order Laue zone (ZOLZ) will be around 0.5 Å (Fig. 1a–c).

For any tilted beam configuration, the diffracted beams will form an off-axis diffraction pattern shifted away from

---

*Corresponding author.
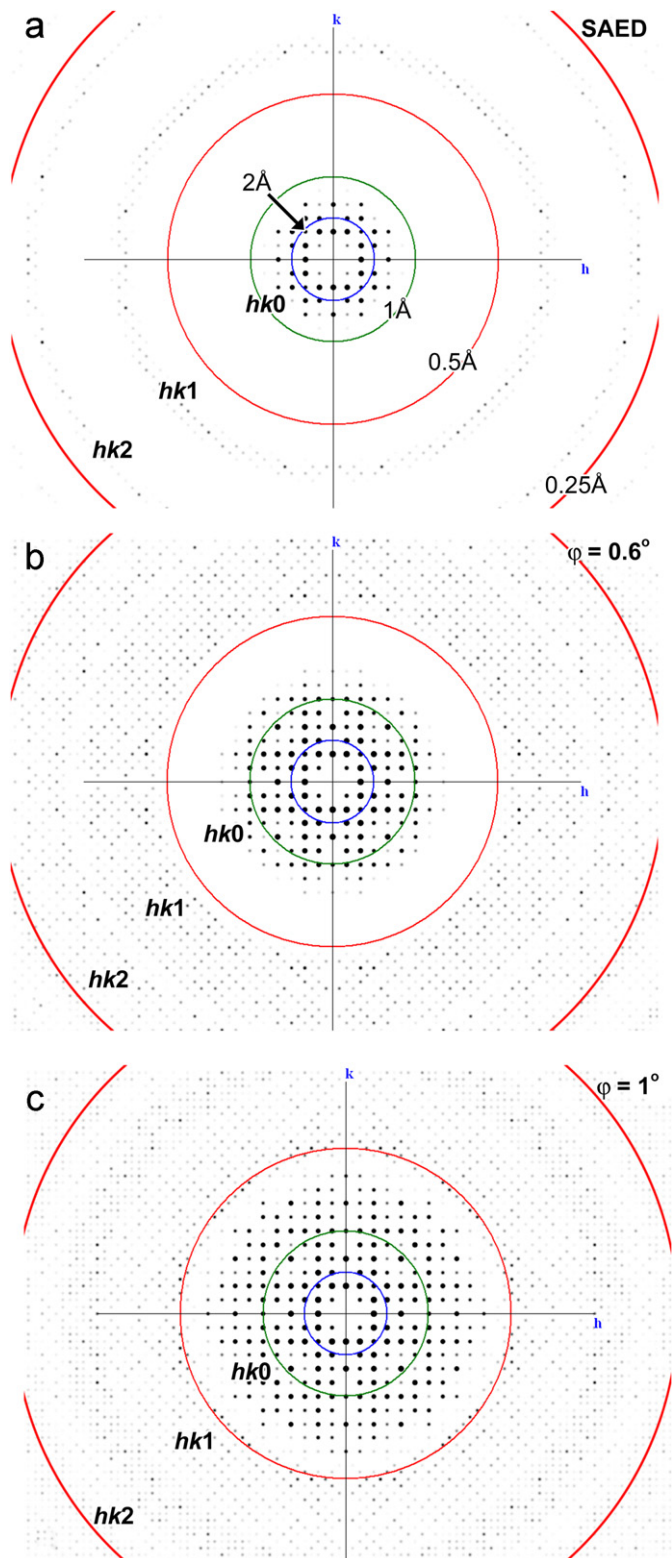 *E-mail address:* oleyniko@struc.su.se (P. Oleynikov).

Fig. 1. Simulated kinematical electron diffraction patterns at 200 kV [0 0 1] zone axis of the mineral uvarovite (cubic, $a = b = c = 12.0065(1)$ Å, Ia$\bar{3}$d, thickness $t = 100$ Å): (a) normal selected area; (b) precession at 0.6° and (c) precession at 1° electron diffraction patterns. Forbidden reflections are absent. Although the FOLZ (h k 1) and SOLZ (h k 2) interpenetrate at this precession angle, the diffraction spots do not overlap due to the systematic absences $h + k + l = 2n + 1$.

the non-tilted beam configuration. Thus, the diffraction pattern will oscillate during precession. It is necessary to de-scan the diffracted beams in a complementary way so that the spots will be in the same positions on the resulting pattern as on a zone-axis diffraction pattern.

The following aspects of precession electron diffraction patterns can be emphasised:

- the resolution is higher than in conventional electron diffraction. This allows collection of more reflections in the ZOLZ and in the high-order Laue zones (HOLZs);
- HOLZ reflections can be illuminated which allows collection of larger 3D data sets;
- the dynamical effects are reduced due to the off-axis beam inclinations because less beams are simultaneously excited;
- indexing of a precession diffraction pattern can be performed in the usual way;
- there is no need for perfect zone orientation during recording of a precession pattern. Quite symmetrical precession patterns are obtained also for off-zone orientation tilted by less than 1°;
- precession electron diffraction patterns contain integrated intensities of the reflections.

Several problems arise during processing precession diffraction patterns. They include:

- overlaps between Laue zones are possible for high precession angles;
- Lorentz correction factors must be applied to the extracted intensities in order to obtain accurate structure factor amplitudes;
- there are no available software packages which take into account all aspects of precession diffraction patterns for indexing and symmetry determination using the information from HOLZ patterns;
- simulation of geometry for precession diffraction patterns is often required. There are three such programs available today: JECP/ED (Java-based, *free*, [8]), ELECTRON DIFFRACTION (*commercial*, J.P. Morniroli [9]) and *JEMS* (Java-based, *commercial*, [10]). *JEMS* can also calculate the intensities [11].

2.1. Precession simulation

One purpose of precession simulation is to help estimating the best conditions for the experiments, especially in cases when an overlap of first-order Laue zone (FOLZ) with ZOLZ is possible. Among other purposes, the following can be emphasized:

- the estimation of intensities, especially the intensities of forbidden reflections;
- the calculation of intensities of diffracted beams as accurately as possible.

Some requirements of precession geometry calculations are:

- the simulation must be able to calculate the visibility of reflections in each layer of the reciprocal lattice;
- the simulation must take the excitation error into account, in order to include all reflections that can possibly be visible on the experimental precession pattern;
- the geometry simulation part must provide the possibility to change the precession angle in run time in order to see changes in the simulated precession pattern;
- the intensities simulation part must include the geometry correction factors for the pure kinematical scattering, in order to obtain the intensities of the kinematical precession electron diffraction pattern;
- the dynamical (multislice) calculation part could be used for the estimation of observed intensities, especially of forbidden or strong reflections;
- the simulation must produce a pattern for any specified zone axis.

All these requirements were carefully analysed and then implemented in the eMap software package [12]. A detailed theoretical description of the models used in the simulations is presented below.

2.1.1. Simulation of precession diffraction patterns

In the conventional SAED mode, the HOLZ can be observed as thin rings of reflections (see Fig. 1a). The number of reflections on these rings depends mainly on the crystal thickness. During precession, when a zone axis is aligned to be parallel to the optical axis of the electron microscope, the zero layer expands into a circular area and the HOLZ reflection rings become annuli (see Ref. [1] and Fig. 1b–c). This expansion depends on the precession angle φ. In case of large real space unit cell (short distances between reciprocal layers with unit cell dimensions $\geqslant 10\,\text{Å}$) overlapping of Laue zones can occur. For example, in the case of uvarovite (cubic, $a = b = c = 12.0065(1)\,\text{Å}$, $Ia\bar{3}d$) the second-order Laue zone (SOLZ) comes very close to the FOLZ already at $0.6°$ precession angle (see Fig. 1b). At

$1°$ precession angle, the FOLZ is very close to the ZOLZ while the SOLZ and FOLZ penetrate into each other (see Fig. 1c).

The differences in periodicities and shifts between reflections in ZOLZ and HOLZ are very easy to detect on these patterns and they can be used to identify the Bravais lattice and the presence or absence of glide planes as described in Ref. [13].

The geometry defining inner and outer radii, $R_{n,\text{in}}$ and $R_{n,\text{out}}$ respectively, for reflections in the layer n of the reciprocal lattice is shown in Fig. 2. The overlapping problem becomes more severe with lower accelerating voltage and with larger unit cell dimension along the electron beam. Notice how the number of recorded diffraction spots increase with precession angle. At $> 0.6°$ precession the FOLZ $(h\,k\,1)$ and SOLZ $(h\,k\,2)$ will interpenetrate. At $> 1.0°$ also the ZOLZ $(h\,k\,0)$ and FOLZ $(h\,k\,1)$ will interpenetrate.

The Laue circles rotate around the zone axis making rings with radii defined

$$R_{n,\text{in/out}} = \sqrt{K^2 - (K_Z - nD)^2} \mp K \sin \varphi, \tag{1}$$

where K is the amplitude of the wave-vector $\boldsymbol{K}$, K_Z is the projection of $\boldsymbol{K}$ on the vertical z-axis.

In case of $n = 0$ we obtain $R_{0,\text{in}} = 0$ and $R_{0,\text{out}} = 2K\sin(\varphi)$ as expected for the ZOLZ. Eq. (1) does not take into account the finite size of the reciprocal nodes, which are elongated in the direction perpendicular to the reciprocal lattice layers. There will be additional reflections visible in each Laue zone due to the finite values of the excitation error s_g, which will extend each annulus.

2.1.2. Precession intensities

The integrated intensities of reflections on a precession diffraction pattern are distorted due to geometrical reasons and crystal thickness. The effect of intensities distortion can be explained by the different ways the Ewald sphere in reciprocal space sweeps through each reflection. The low-angle reflections spend more time close to Bragg conditions than the high-angle reflections. The Ewald sphere sweeps
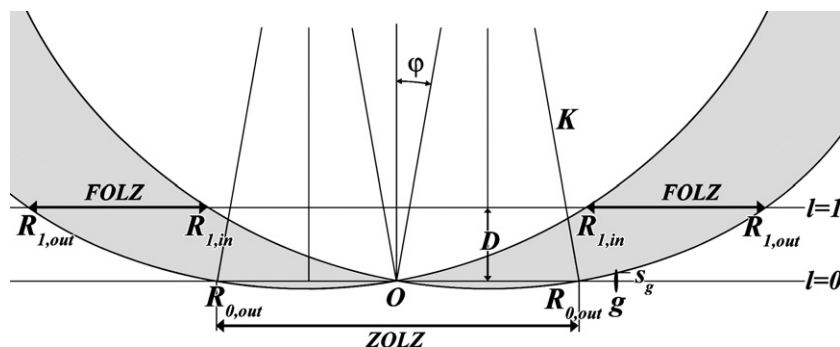

Fig. 2. The precession geometry for intersections of the Ewald sphere with reciprocal lattice layers for a beam incident with the zone axis at the angle φ. O is the origin; $R_{0,\text{out}}$ is the radius of the ZOLZ circular patch; $R_{1,\text{in}}$ and $R_{1,\text{out}}$ are inner and outer radii respectively for the FOLZ annulus; D is the distance between reciprocal layers $l = 0$ and 1; s_g is the excitation error for the $\boldsymbol{g}$ reflection.

through each reflection twice during a full 360° cycle; each time providing integration over the reflection.

2.1.2.1. Two-beam kinematical approach.

The use of two-beam approach requires the knowledge of the structure factors for the given structure, because it is included in Eq. (3) for the extinction distance. The diffracted intensity in terms of kinematical theory in the two-beam case can be expressed by the following equation (see Refs. [14,15]):

$$I_g^{kin} = I \left(\frac{\sin(\pi s_g t)}{\xi_g s_g} \right)^2, \qquad (2)$$

where

$$\xi_g = \frac{\pi \Omega \cos \theta_B}{\lambda F_g} \qquad (3)$$

with ξ_g known as the extinction distance, θ_B is the Bragg angle for the reflection g, Ω is the volume of the unit cell, λ is the electron wavelength, t is the specimen thickness, s_g is the excitation error and F_g is the structure factor for the reflection g.

The first zero occurs at $s_g = 1/t$, and it defines the length of the reciprocal lattice points. These points are, in fact, extended into relrods of length $2/t$ perpendicular to the foil (see Fig. 4).

The integrated intensity of any reflection g on the precession diffraction pattern can be expressed by the following integral:

$$I_g^{prec} = \int I_g^{kin}(s_g) \, ds_g. \qquad (4)$$

Eq. (4) represents the integral of the kinematically scattered intensity over the excitation error s_g. The excitation error depends on the position of the Ewald sphere during precession. In order to express this dependence, the Ewald sphere centre can be represented by

$$K_z = K \cos \varphi,$$
$$K_{xy} = K \sin \varphi, \qquad (5)$$

where K_{xy} is a projection of the wave vector $\boldsymbol{K}$ on the xy plane. Using the current azimuthal position ω of the Laue circle (see Fig. 3), we can express K_{xy} as K_x and K_y components

$$K_x = K_{xy} \cos \omega,$$
$$K_y = K_{xy} \sin \omega. \qquad (6)$$

The final equation, which expresses the dependence of the excitation error on the current Ewald sphere position, is

$$| - K + g + n s_g| = K, \qquad (7)$$

where n is the surface normal. Solving (7) for s_g we get the dependence of the excitation error on the current position ω on the Laue circle

$$s_g(\omega) = K_z - g_z - \sqrt{(K_z - g_z)^2 + 2K(\omega)g - g^2}, \qquad (8)$$

where g_z is the z-component of the vector g.

In the assumption that $K_z \approx K$ and $g \ll K$, we can expand the square root into a series, which will reduce (8) to the well-known equation for the excitation error (see Ref. [14]):

$$s_g = \frac{g^2 - 2Kg}{2K} \qquad (9)$$

and then simplified to

$$s_g = \frac{g^2}{2K} - [g_{xy}\varphi \cos(\alpha - \omega) + g_z]. \qquad (10)$$

The last equation is a very good approximation for the excitation error for any given g vector and small precession angles (up to 3–4°). It is valid for HOLZ as well as for ZOLZ. This equation can be used in calculations of the correction factor for the integrated intensities.

In order to visualize Eq. (8), we can take a look at an artificial example with a periodicity along the a^*-axis of $0.2 \, \text{Å}^{-1}$ in reciprocal space. Let us consider the precession angle $\varphi = 3°$ and the accelerating voltage $E_a = 200 \, \text{kV}$. The dependence of the excitation error s_g for a reflection $g = 4\,0\,0$ on the angle ω is shown in Fig. 5a.

Finally, the integrated intensity of the spot g can be expressed as the integral over the angle ω as follows:

$$I_g^{prec} = \int_0^{2\pi} I_g^{kin}(s_g(\omega)) \, d\omega, \qquad (11)$$

$$I_g^{prec} = I \int_0^{2\pi} \text{oscill}(s_g(\omega)) \, d\omega = I A_{corr}, \qquad (12)$$

where oscill is the oscillation function $(\sin(\pi s_g t)/\pi s_g t)^2$ (see Fig. 4).

The dependence of the intensity of the reflection $g = 4\,0\,0$ on the position of the precessing beam is shown in Fig. 5b. The correction coefficient can be calculated for each
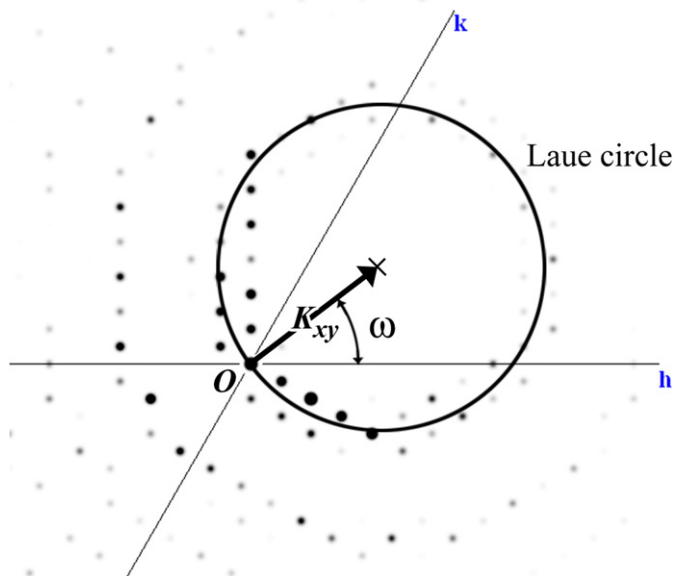

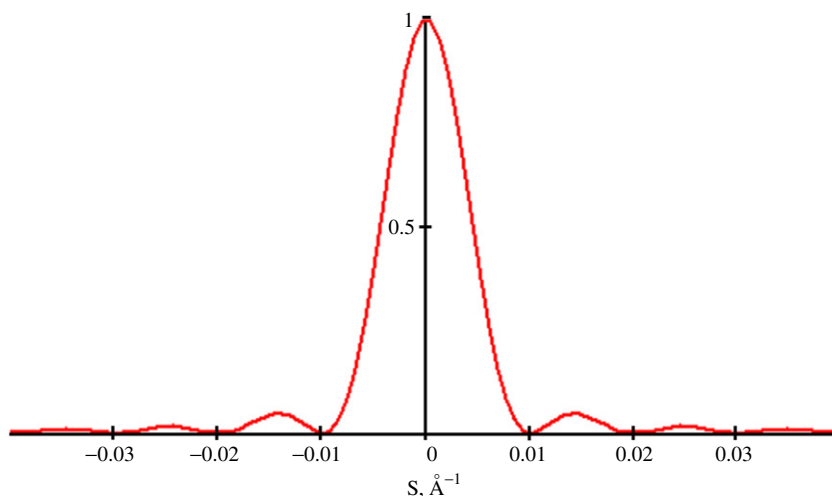Fig. 3. The azimuthal position ω of the Laue circle during precession. O is the lattice origin.

Fig. 4. The intensity oscillation function $\left(\sin(\pi s_g t)/\pi s_g t\right)^2$ for a foil of thickness $t = 100\,\text{Å}$.
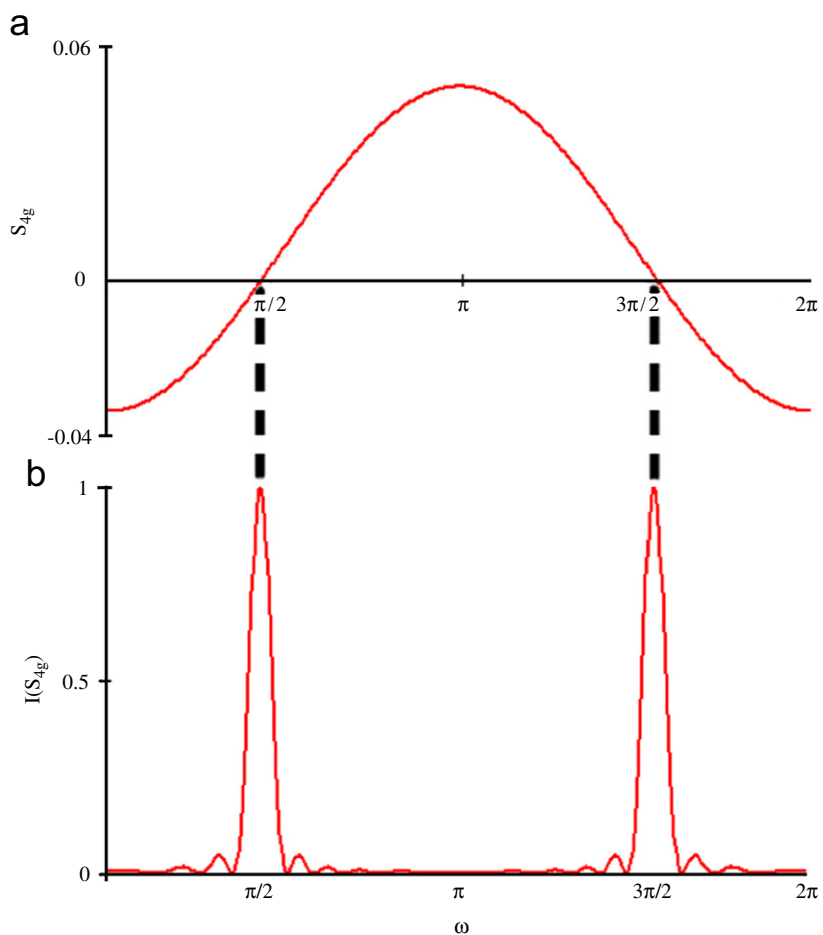

Fig. 5. (a) The dependence of the excitation error s_g for a reflection $\boldsymbol{g} = 400$ on the angle ω; (b) the dependence of the intensity oscillation function on the angle ω for a foil of thickness $t = 100\,\text{Å}$.

reflection $\boldsymbol{g}$. The values of correction coefficient A_{corr} for a row of reflections from $\boldsymbol{g} = 100$ up to $\boldsymbol{g} = 3000$ is shown in Fig. 6.

The precession geometry is quite complicated, which results *inter alia* in an increase of observed intensities for reflections at the outer radius of the precession pattern, as
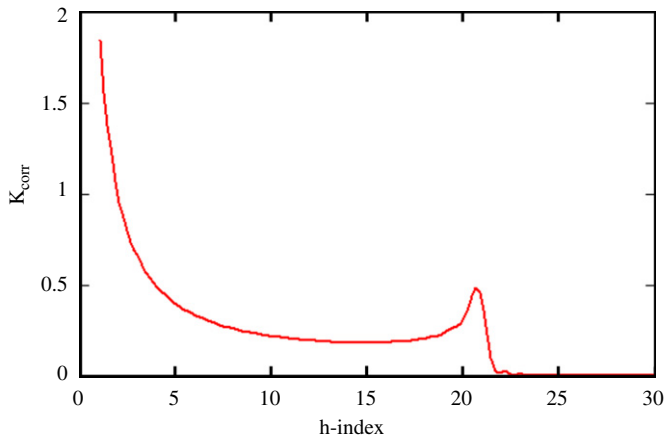
Fig. 6. The correction coefficient A_{corr} values for the row of $h00$ reflections for a 100 Å thickness.

shown in Fig. 6. The spots with h-indices 1–4 lie very close to the Ewald sphere at all beam tilts, which explains high values of A_{corr} close to the origin.

The local maximum of A_{corr} near the 21st h-index can be explained using the value R_L of the Laue circle radius for the current precession configuration ($\varphi = 3°$, $E_a = 200\,\text{kV}$, $a^* = 0.2\,\text{Å}^{-1}$), which is $2.093\,\text{Å}^{-1}$. The 21st reflection has $|\mathbf{g}| = 4.2\,\text{Å}^{-1}$ and lies very close to the value of $2R_L$ which is the diameter of the Laue circle (same as $R_{0,out}$ in Fig. 2). Thus the reflection $2\,1\,0\,0$ spends more time close to the Ewald sphere than its neighbours during precession.

2.1.2.2. Two-beam dynamical approach. Introducing the effective excitation error for the two-beam dynamical theory (see Ref. [16])

$$s_{g,\text{eff}} = \sqrt{s_g^2 + \frac{1}{\xi_g^2}}, \tag{13}$$

we can calculate A_{corr} values for the two-beam case, which assumes that only one beam other than the incident is strongly excited. The profile of $I_g^{2\text{-beam}}$ depends on the extinction distance and can show several maxima ($\xi_g \ll t$) as well as a single.

2.1.2.3. Many-beam approach. Many-beam dynamical theory extends the two-beam theory and requires a computer for their solution. The solution of the many-beam theory eigenvalue equation, the so-called secular equation, will provide eigenvalues and eigenvectors, which completely specify the diffracted beam amplitudes for a crystal at any given thickness t.

Another approach to obtain the dynamical amplitudes for diffracted beams at a given thickness is the multislice method.

In both cases, when simulating precession, the calculations must proceed with many incident beam tilts, which will cover the full circle. This can be a time-consuming process due to the extension of dimensions in reciprocal plane, which must include more beams to a very high resolution, especially for high precession angles. The total time can be estimated as $N_{tilts} \cdot N_{slices}\,(t_{FFT} + t_{IFFT})$, where N_{tilts} is the total number of beam tilts in the precession simulation, N_{slices} is the total number of slices to be calculated for the given thickness, t_{FFT} and t_{IFFT} are the times needed to calculate Fast Fourier Transform (FFT) and Inverse FFT, respectively. Obviously, the total time will be N_{tilts} times longer than it is required for the conventional multislice method.

2.1.3. R-factors

In order to reach reasonable R-factor values one can use a structure refinement method, which will take the dynamical scattering into account. There are two methods developed for the simulation of electron diffraction intensities from dynamically scattering samples: Bloch waves [17,18] and multislice methods [19]. There are only two programs *MSLS* [20] and *NUMIS* [21] available for the refinement of dynamical intensities, which use the multislice (or so-called image-based) approach.

All beams in experimental selected-area electron diffraction patterns are affected by thickness and orientation. Unfortunately, these may vary in a complicated non-linear way across the illuminated specimen in SAED and in precession, because the illuminated area is typically $>20\,\text{nm}$. The experimental data quite often do not match too well with simulated patterns calculated assuming one average experimental thickness and orientation.

Electron diffraction data collected with precession will be less affected by dynamical effects. It is hoped that this will make it possible to reach lower R-values, i.e. better correspondence between observed and calculated intensities. Today R-values for electrons are at the 15–20% level [22] but we would like to reach 5–10% as in X-ray crystallography.

3. Applications: simulation of precession electron diffraction patterns

The quality of simulated precession patterns was evaluated by comparison with experimental data. Precession patterns were calculated using the multislice method in order to take the dynamical interactions into account. The experimental precession electron diffraction pattern was taken from $Cs_{0.44}Nb_{2.54}W_{2.46}O_{14}$ with the space group Pbam and unit cell parameters $a = 27.145(2)\,\text{Å}$, $b = 21.603(2)\,\text{Å}$ and $c = 3.9463(3)\,\text{Å}$ [23,24].

3.1. Experiment

An experimental precession pattern was taken near the $[0\,0\,1]$ zone axis of $Cs_{0.44}Nb_{2.54}W_{2.46}O_{14}$ by Joaquim Portillo on a Philips EM400 TEM operated at $100\,\text{kV}$ equipped with the commercial precession system CASTEL/ SPINNING STAR (NanoMegas Company). The pattern was recorded on DITABIS imaging plates, having high

dynamical range (16-bit greyscale). The precession angle was 2.73° (47.6 mrad). No HOLZ reflections were observed during the experiment.

3.2. Simulation

Precession electron diffraction patterns were simulated for the [0 0 1] projection using the multislice method [19] implemented in the eMap programme. The atomic coordinates used were those given in Ref. [24]. Isotropic atomic displacement parameters U of 0.05 Å^2 and 0.07 Å^2 were assigned to metal and oxygen atoms, respectively.

Twenty-eight precession patterns were simulated with thicknesses from 60 up to 600 Å with steps of 20 Å. Each simulated precession pattern was calculated as a sum of 250 diffraction patterns, i.e. with azimuthal steps 1.44° apart around a full circle. The resolution of the simulation was 0.11 Å to take into account multiple diffraction from high-g beams back into the central beams.

Simulated intensities were compared with the experimental precession pattern. The experimental intensities I_{hkl} of reflections were estimated using the ELD programme [25,26]. The intensities were merged according to the p2gg plane group resulting in 683 unique $hk0$ reflections within a resolution of 1.0 Å. 43 axial $h00$ and $0k0$ reflections were kinematically forbidden, but due to the dynamical scattering they had small but finite intensities (see Figs. 7 and 8). The internal R-factor of symmetry-related reflections in the merged experimental data set was 13.9%. Experimental and simulated precession electron diffraction patterns are shown in Fig. 7.

3.3. Effects of precession on rows of forbidden reflections

Three different beam tilts during the precession are shown in Fig. 8. While the systematically forbidden reflections ($h = 2n + 1$) along the $h00$ line are really absent in Fig. 8a and b with 0° beam azimuth, intensity can be seen in some of the forbidden reflections along $0k0$. The finite intensities of 050 and 090 reflections are due to multiple scattering. The opposite situation can be seen at the 90° beam azimuth position (the beam is tilted along $0k0$ direction) as shown in Fig. 8c and d. Here the reflections 300, 500, etc. along the $h00$ line have finite intensities, while the reflections with $k = $ odd in the $0k0$ row are now absent. This behaviour can be explained as follows. The $0k0$ ($k = $ odd) reflections are kinematically forbidden owing to a b-glide perpendicular to the a-axis. The following relations exist between the crystal structure factors:

$$F(h\,k\,0) = F(\bar{h}\,k\,0) \quad \text{for } k = 2n \text{ (even)},$$

$$F(h\,k\,0) = -F(\bar{h}\,k\,0) \quad \text{for } k = 2n + 1 \text{ (odd)}.$$

When the centre of the Laue circle lies on the axis k, all possible paths of waves which end in any kinematically forbidden reflection on this axis will have the same but "mirrored" path with a wave of exactly the same amplitude
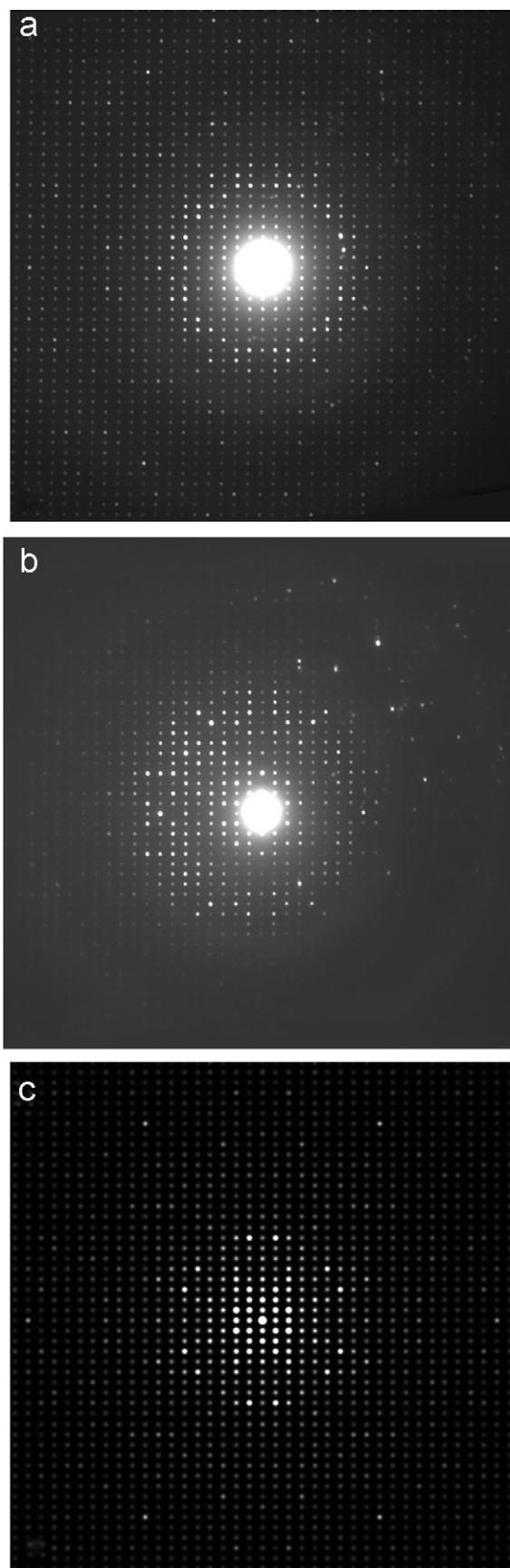
Fig. 7. Electron diffraction patterns of $Cs_{0.44}Nb_{2.54}W_{2.46}O_{14}$: (a) experimental precession, (b) the experimental SAED (courtesy J. Portillo and T.E. Weirich) and (c) simulated precession at 200 Å thickness.
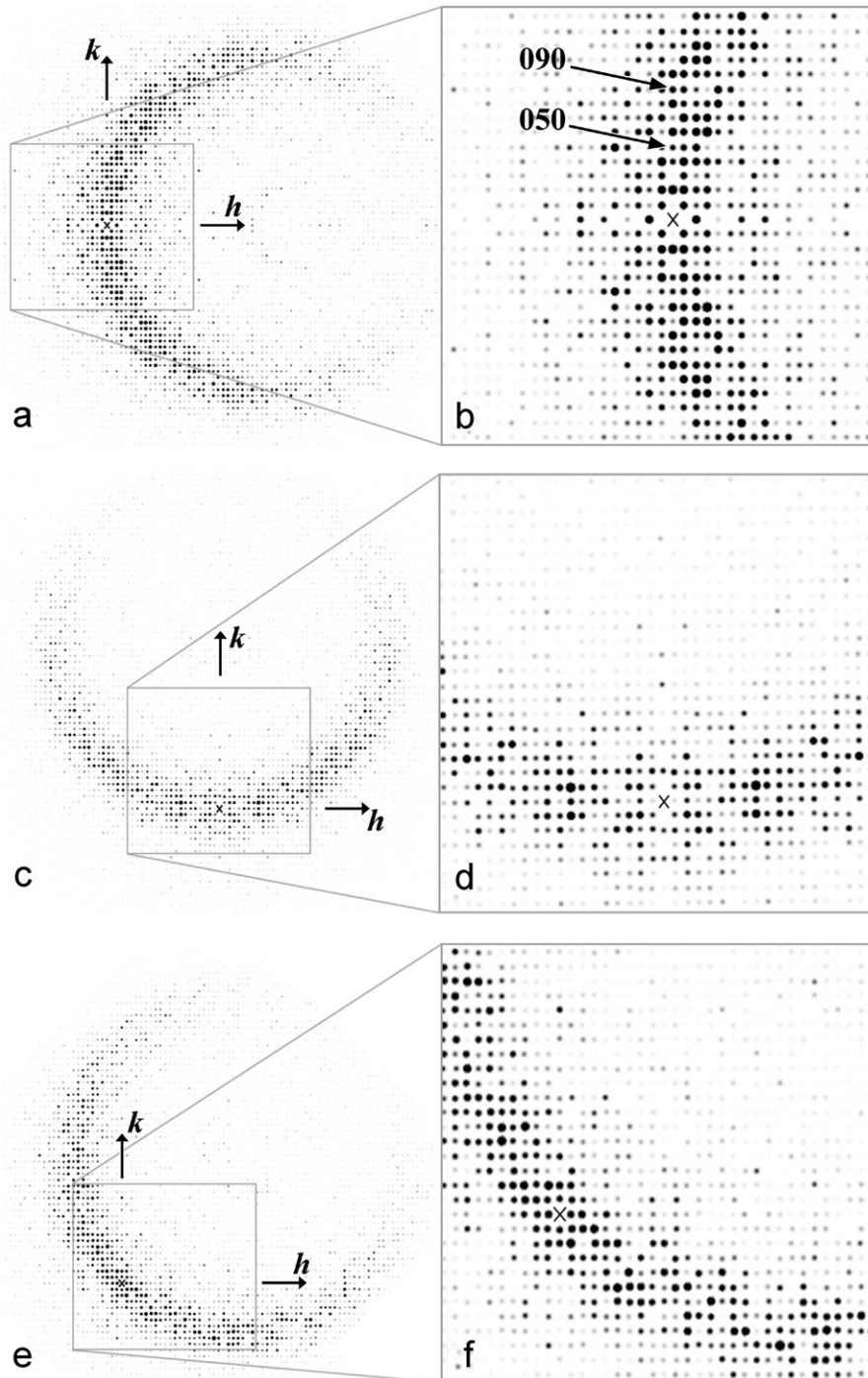
Fig. 8. Three different beam tilts during precession with the angle of 2.73°. The tilts are: (a) along the *h*-axis (azimuth 0°); (c) along the *k*-axis (azimuth 90°); (e) in a diagonal direction (azimuth 45°). (b), (d) and (f) central parts enlarged. Some forbidden axial reflections have some intensity due to dynamical scattering, such as 050 and 090 in (b).

but opposite sign and thus they cancel each other. A similar situation is for a Laue centre, which lies on the *h* axis when there are forbidden reflections *h*00, *h* = odd.

The situation shown in Fig. 8e and f is different from both cases of perfect beam tilts along either *h*00 or 0*k*0 main axes. A precession pattern is the sum of patterns with the beam tilt (azimuth) going around the full circle from 0°

to 360°. In most of these directions systematically forbidden axial reflections will get some intensity. Thus the kinematical rules are not valid and both main axes lines show some intensity of kinematically forbidden reflections.

In case of $Cs_{0.44}Nb_{2.54}W_{2.46}O_{14}$, the experimental precession diffraction pattern shows quite strong intensities of kinematically forbidden reflections along *h*00 and 0*k*0 rows
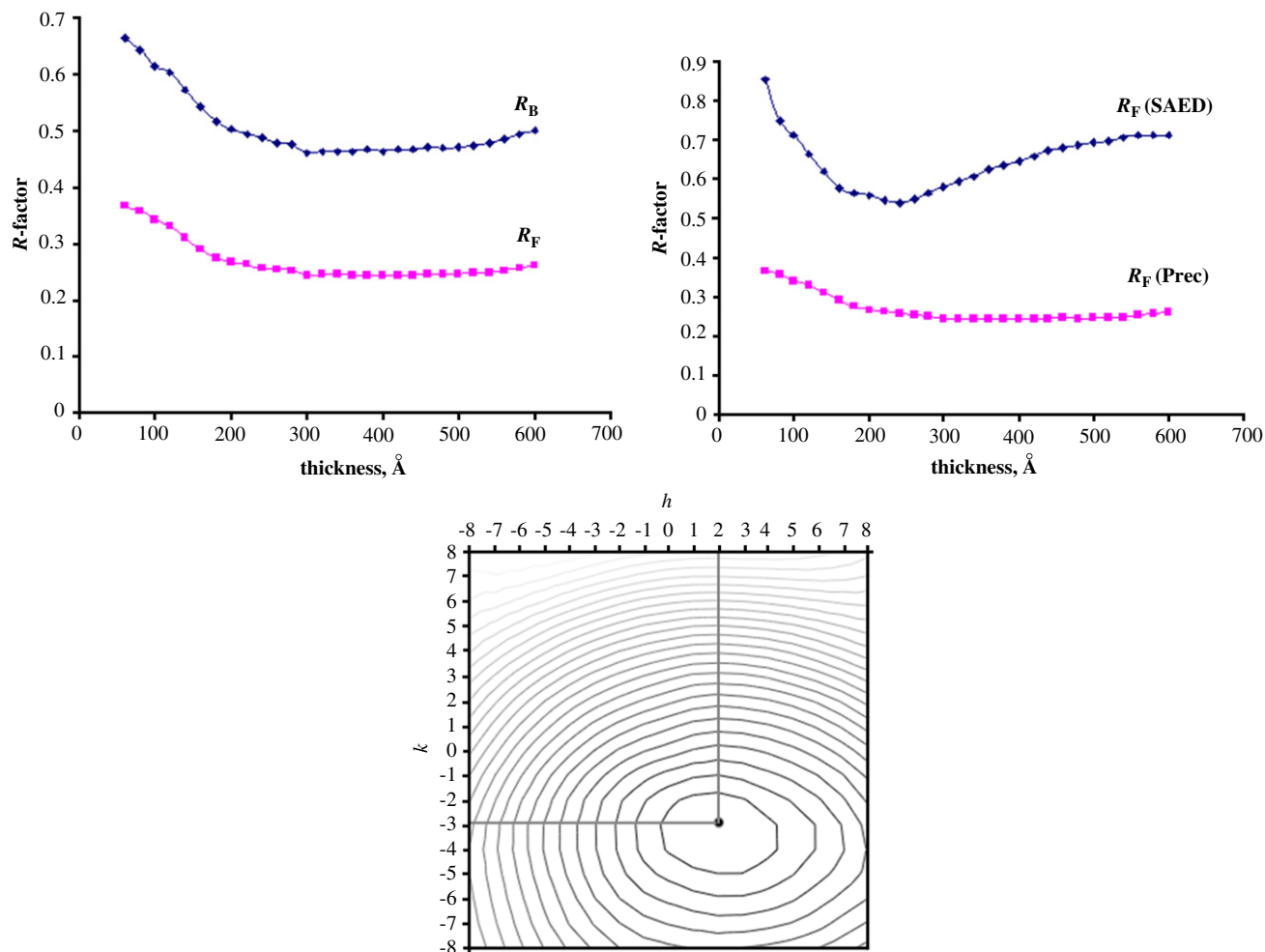
Fig. 9. The dependence of R factors on the thickness in (a) the dynamical (multislice) simulation (R_F and R_B are defined in the text), (b) multislice precession (Prec) and multislice SAED R_F factors. (c) The contour plot of the R_F factor for the crystal tilt estimation. The minimum of R_F corresponds to the Laue circle centre at $h = 2$ and $k = -3$.

while the same reflections are very weak on the SAED pattern. This behaviour can be explained by the discourse made above. Among all possible Laue point positions, there are only four incident beam positions (two for each of the main axes directions) where dynamical interactions do not affect kinematically forbidden reflections. All other beam tilts will give rise to forbidden reflections. Due to the integration over the excitation error during the precession experiment, these forbidden reflections can be strongly influenced by dynamical scattering. In case of close spacing of reciprocal points, this effect can be even more pronounced than in an SAED pattern. A perfectly aligned SAED pattern should not have any intensity in forbidden axial reflections according to the argument above. This situation can be observed as Gjønnes–Moodie lines (see Ref. [27]) present in the forbidden reflections when the incident beam is parallel to a glide plane or perpendicular to a screw axis in CBED experiment. In practice, it is not possible to achieve perfect conditions for the SAED pattern, such as perfect alignment and perfect crystal shape, etc., and thus there will always be some intensity in

those forbidden reflections. However, this is not the case when the unit cell parameters are small (for example, 5.43 Å as in pure silicon, as noticed in Ref. [24]), which leads to large spacing between reciprocal points and as a result the kinematically forbidden reflections will rise much less in precession patterns.

3.4. Effects of precession for general reflections

On the other hand, dynamical scattering effects are in general significantly reduced for general reflections, such as $hk0$ with both $h \neq 0$ and $k \neq 0$. This can be explained if we take a look at the total number of beams, which are close to Bragg condition simultaneously at every Laue circle position during the precession. The total number of possible paths, due to double scattering, is reduced significantly in case of precession. In summary, dynamical scattering effects have less influence on the integrated intensities of most reflections in precession than in SAED patterns. The relatively poor performance on system-atically forbidden axial reflections, as discussed in Section

3.3, is not very serious; if the odd reflections are much weaker than the even ones, we can still identify the symmetry element (2, screw axis and glide planes). Forbidden reflections are then eliminated in the calculations.

3.5. Quantification

The intensities obtained from simulated SAED and precession patterns (Fig. 7c) were compared to the experimental SAED (Fig. 7b) and precession patterns (Fig. 7a), using both R_F and R_B.

R_F is defined as

$$R_F = \frac{\sum_k ||F_{k,\text{obs}}| - |F_{k,\text{calc}}||}{\sum_k |F_{k,\text{obs}}|} \tag{14}$$

and R_B

$$R_B = \frac{\sum_k |I_{k,\text{obs}} - I_{k,\text{calc}}|}{\sum_k I_{k,\text{obs}}} \tag{15}$$

As usual in electron diffraction, the exact thickness range of the specimen is not known. Thus precession patterns were simulated for a large range of thicknesses. R_B and R_F were calculated for each thickness as shown in Fig. 9a for the precession simulation. These factors are calculated without any refinement using the model obtained from the Rietveld refinement of X-ray powder diffraction pattern [24]. The R-factors have a clear flat minimum, which lies within a very broad range of thicknesses from 300 up to 580 Å. If there is a possibility to use CBED or EELS methods then it can be possible to have an idea of the thickness, which will reduce the total number of multislice simulations.

4. Conclusion—do precession patterns give better intensities than SAED?

The R_F factor for multislice precession simulation was much better (i.e. smaller) than the R_F factor for multislice SAED (see Fig. 9b).

After the LS refinement the R_F factor reported in Ref. [24] was 39.2%. In case of multislice SAED, both the thickness and beam tilt were varied. It should be noted that there was no refinement of any structural parameters during these simulations. The estimated crystal tilt position was $h = 2$, $k = -3$ (see Fig. 9c). SAED patterns were then simulated at this tilt, with thicknesses ranging from 50 to 600 Å. The lowest R_F value was 52% at $t = 240$ Å.

The R_F factor for the pure kinematical precession simulation data was 25%, which is almost as good as the minimum value of 24.3% for the multislice precession simulation. Thus intensities in precession electron diffraction patterns are less dynamical than are intensities in SAED patterns. We may expect that the R_F value of the precession patterns may drop further with a structure refinement taking dynamical effects into account.

This behaviour is as expected, but the fact that we do not get down under 20% R-value even when doing multislice simulations, shows that there are still some factors that are not completely understood or under control. These may include effects of crystal thickness variation of the selected area, slight misalignments of the crystal, the fact that the inelastically scattered electrons are not included in the calculations, errors in electron scattering factor tables (may be $\pm 10\%$), unclear scattering factors of charged atoms (especially the negatively charged oxygen atoms), errors in data acquisition (overflow of strongest reflections) and errors in data extraction by ELD, etc. But all taken together, we can say that these results are quite good, considering that electron crystallography is newer and less developed than X-ray crystallography and that the electron scattering is so much stronger (and thus more complicated) than X-ray scattering. New hardware (including the precession technique and CCD and imaging plate detectors) and software developed as part of this work provide tools for electron crystallography. These will facilitate further work towards a better understanding of the theory of electron scattering and improved practical procedures, leading to more exact results in electron crystallography in the near feature.

In this work we used a structure with relatively large unit cell parameters a and b. It would be interesting to see the behaviour of calculated intensities in precession geometry using multislice simulation for smaller unit cells. In our further work we will use the precession simulations and compare with experimental data for other structures, including some that have small unit cell parameters.

References

[1] R.J. Vincent, P.A. Midgley, Ultramicroscopy 53 (3) (1994) 271.
[2] J. Gjønnes, V. Hansen, B.S. Berg, P. Runde, Y.F. Cheng, K. Gjønnes, D.L. Dorset, C.J. Gilmore, Acta Crystallogr. A 54 (1998) 306.
[3] M. Gemmi, X.D. Zou, S. Hovmöller, A. Migliori, M. Vennström, Y. Andersson, Acta Crystallogr. A 59 (2003) 117.
[4] K. Gjønnes, On the integration of electron diffraction intensities in the Vincent–Midgley precession technique, Ultramicroscopy 69 (1) (1997) 1–11.
[5] K. Gjønnes, Y.F. Cheng, B.S. Berg, V. Hansen, Corrections for multiple scattering in integrated electron diffraction intensities, Application to determination of structure factors in the [001] projection of AlmFe. Acta Crystallogr Section A 54 (1998) 102–119.
[6] C.S. Own, System Design and Verification of the Precession Electron Diffraction Technique, Department of Materials Science and Engineering, Northwestern, Evanston, 2005 p. 161.

[7] C.S. Own, L.D. Marks, W. Sinkler, Precession electrondiffraction 1: multislice simulation, Acta Crystallogr A 62 (2006) 434–443.

[8] X.Z. Li, J. Appl. Crystallogr. 36 (2003) 956.

[9] J.P. Morniroli, Electron diffraction, e-mail: jean.paul.morniroli@univ-lille1.fr, 2003.

[10] P. Stadelmann, JEMS—EMS Java version, CIME-EPFL, CH-1015 Lausanne, 2004.

[11] P. Stadelmann, GUMP Conference, Lille, France, 16–17 November 2005.

[12] P. Oleynikov, eMap, e-mail: oleyniko@struc.su.se.

[13] J.P. Morniroli, J.W. Steeds, Ultramicroscopy 45 (1992) 219.

[14] B.K. Vainshtein, B.B. Zvyagin, A.S. Avilov, in: J.M. Cowley (Ed.), Electron Diffraction Techniques, vol. 1, IUCr, 1992, pp. 117–312.

[15] J.C.H. Spence, J.M. Zuo, Electron Microdiffraction, Plenum Press, New York, 1992.

[16] J.M. Cowley, Diffraction Physics, Elsevier Science Publishers B.V., Amsterdam, 1986.

[17] L. Sturkey, Acta Crystallogr. 10 (1957) 858.

[18] H. Niehrs, Z. Phys. 156 (1959) 446.

[19] J.M. Cowley, A.F. Moodie, Acta Crystallogr. 10 (1957) 609.

[20] J. Jansen, D. Tang, H.W. Zandbergen, H. Schenk, Acta Crystallogr. A 54 (1998) 91.

[21] NUMIS, internet link: ⟨http://www.numis.northwestern.edu/Facilities/Computers/numis.shtml⟩.

[22] T.E. Weirich, R. Ramlau, A. Simon, X.D. Zou, S. Hovmöller, Nature 382 (1996) 144.

[23] M. Lundberg, M. Sundberg, Ultramicroscopy 52 (1993) 429.

[24] T.E. Weirich, J. Portillo, G. Cox, H. Hibst, S. Nicolopoulos, Ultramicroscopy 106 (3) (2006) 164.

[25] X.D. Zou, Y. Sukharev, S. Hovmöller, Ultramicroscopy 49 (1993) 147.

[26] X.D. Zou, Y. Sukharev, S. Hovmöller, Ultramicroscopy 52 (1994) 436.

[27] J. Gjønnes, A.F. Moodie, Acta Crystallogr. 19 (1965) 65.